

Effect of Temperature on the Fracture Toughness of a NiTiHf High Temperature Shape Memory Alloy

B. Young^a, B. Haghgouyan^a, D.C. Lagoudas^{a,b} I. Karaman^{a*}

^a Department of Materials Science and Engineering, Texas A&M University, College Station, 77843 TX, USA

^b Department of Aerospace Engineering, Texas A&M University, College Station, 77843 TX, USA

*: Corresponding author: ikaraman@tamu.edu

Abstract

The fracture toughness of $\text{Ni}_{50.3}\text{Ti}_{29.7}\text{Hf}_{20}$ high temperature shape memory alloy (HTSMA) was systematically investigated as a function of temperature. A set of nominally isothermal fracture toughness tests were conducted on disk-shaped compact tension specimens at five temperatures corresponding to three thermodynamical conditions: (i) below martensite finish temperature M_f to obtain the fracture toughness of martensite, (ii) above martensite start temperature M_s in austenite, but below the martensite desist temperature M_d (the temperature above which austenite does not transform), in order to find the fracture toughness when stress induced martensitic (SIM) transformation takes place close to the crack tip, and (iii) above M_d , in order to obtain the fracture toughness of austenite. The extent of the inelastic zone near the crack tip was detected using digital image correlation, and the fracture surfaces were examined. The fracture behavior was highly temperature/phase dependent. The fracture toughness of the transforming material was higher than that of austenite and martensite, i.e. SIM transformation acts as a toughening mechanism. This was attributed to the differences in strain hardening behavior in detwinning, martensitic transformation, and plastic deformation regimes of the stress-strain response, where SIM transformation occurs with the lowest strain hardening rate. The fracture toughness values obtained here are lower than those of equiatomic NiTi

Keywords: Fracture toughness; High temperature shape memory alloys; NiTiHf; Phase transformation

1. Introduction

Shape Memory Alloys (SMAs) are high energy density active materials that can undergo repeatable and reversible macroscopic shape changes due to martensitic phase transformation [1]. Since SMAs feature a very high work output for a specific volume as compared to active materials [1], they are promising candidates for replacing existing actuators (e.g. hydraulic or electromagnetic) in weight critical applications

[2, 3]. Nickel-titanium (NiTi) is the most commonly known and commercially available SMA, and has seen widespread use in the biomedical industry due to its good biocompatibility, corrosion resistance, and superior mechanical properties [4]. However, the low transformation temperatures of NiTi SMAs have limited their applications as actuators, especially in the aerospace industry, which requires high temperature, actively-controlled actuators. Adding ternary alloying elements to NiTi increases the transformation temperatures to a useable range [5, 6]. In particular, NiTiHf high temperature shape memory alloys (HTSMAs) have been widely explored through several studies focusing on microstructural analysis [7-17], mechanical properties [18-21], fatigue life [22-26], and the effect of processing parameters on microstructure and properties [27-29]. Moreover, the practical viability of NiTiHf HTSMAs has been demonstrated on a test flight as part of an adaptive aircraft structure [30]. However, successful employment of NiTiHf HTSMAs in such applications requires a complete understanding of their crack growth behavior and precise quantification of their fracture properties. To the best of the authors' knowledge, there is no work in the literature reporting fracture toughness of NiTiHf based HTSMAs in the temperature range that covers all possible material states. Moreover, it is not clear whether these ternary SMAs are tougher than NiTi binary alloys or not.

In literature, the majority of studies on the fracture of SMAs [31-41] have reported the fracture toughness of NiTi using ASTM E399 [42], which is based on Linear Elastic Fracture Mechanics (LEFM). However, most of the reported experiments in such studies do not satisfy the small-scale yielding condition, which is required for the validity of LEFM. Additionally, because the presence of phase transformation alters near-tip mechanical fields [43-48], SMAs do not conform to conventional elasto-plasticity, and therefore Elasto-Plastic Fracture Mechanics (EPFM) cannot be used to characterize the crack growth behavior and predict fracture in SMAs. Recently, there have been efforts [49, 50] to obtain the fracture properties of NiTi using the full-field displacement data, obtained from digital image correlation (DIC). Unlike the standard testing methods, which are used to determine the fracture toughness from load-displacement data, this method requires relatively sophisticated testing setup and rigorous post processing. In an attempt to address some of these challenges, a new methodology described in [51] modifies the existing ASTM E1820 standard [52] to take into account the transformation- and reorientation-induced changes in the elastic properties.

Because the constitutive response of the SMAs is sensitive to temperature, even small variations in temperature may further complicate the study of their fracture behavior. Consequently, quantifying fracture properties of SMAs can be challenging compared to conventional metals. Although fracture properties of NiTi SMAs have been reported in many studies over the years, there seems to be a lack of consensus on the effects of temperature/phase transformation on their fracture toughness [31, 34, 51, 53, 54], in particular

on whether martensitic transformation provides a toughening effect or not. For example, Holtz *et al.* [31] and Maletta *et al.* [54] reported that fracture toughness increases monotonically with temperature in NiTi SMAs. However, the results of Gollerthan *et al.* [34] and Haghgouyan *et al.* [51] demonstrated that the fracture toughness of NiTi binary SMAs is a stepwise function, with fully martensitic materials and materials transforming from austenite to martensite having the same fracture toughness, and the austenite phase above martensite desist temperature, M_d , exhibiting higher fracture toughness. Clearly, there is a need to systematically investigate the fracture behavior of new NiTiHf HTSMAs at different temperatures, especially in the martensitic transformation range.

There are only two reported studies on the fracture and crack growth behavior of NiTiHf HTSMAs [55, 56]. In the recent study by the authors, the fracture of an aged martensitic NiTiHf has been investigated under mode-I nominally isothermal loading. Using a disk-shaped compact tension (DCT) specimen, fracture toughness was measured at room temperature (below martensite finish temperature, M_f) [55]. Unstable crack growth was observed due to the limited extent of dissipation mechanisms near the crack-tip. The results showed that the fracture toughness of martensitic NiTiHf is relatively lower than that of binary NiTi SMAs. Amin-Ahmadi *et al.* [56] studied crack propagation mechanisms in an aged NiTiHf HTSMA using post-mortem microstructure characterizations. Transmission electron microscopy (TEM) micrographs showed that cracks propagate mainly along the $\langle 011 \rangle$ type II twin planes, switching between the twin planes to avoid nano-sized H-phase precipitates.

In the present study, we present the first investigation into the fracture toughness of a NiTiHf HTSMA at different temperatures and phases: (i) below M_f in fully martensitic state, (ii) above martensite start temperature, M_s , where the stress induced martensitic (SIM) transformation takes place, and (iii) above M_d in fully austenitic state. Microstructural characterization, near tip strain field measurements, and post-mortem fracture surface analyses have been performed. The fracture toughness values of the NiTiHf HTSMA were determined at five different temperatures. It was observed that the martensite phase exhibits the lowest fracture toughness and SIM transformation provides a significant toughening effect leading to a higher fracture toughness in the martensitic transformation regime than that of both austenite and martensite phases. The deformation and strain hardening behavior observed in the uniaxial tension experiments shed some light into the potential reasons for the observed differences in the evolution of fracture toughness values with temperature.

2. Experimental Methods

2.1 Material

Elemental Ni, Ti, and Hf (99.98%, 99.95% and 99.9% in purity, respectively) were used to fabricate $\text{Ni}_{50.3}\text{Ti}_{29.7}\text{Hf}_{20}$ (at.%) HTSMA via vacuum skull melting under partial argon atmosphere. The material was vacuum homogenized at 1050°C for 72 hours and furnace cooled down to room temperature. Finally, the homogenized ingot was sealed in a mild steel can and hot extruded at 900°C. The transformation temperatures of the hot extruded material were measured using differential scanning calorimetry (DSC) and determined using the intersecting tangent lines method to be $M_f = 125.6^\circ\text{C}$, $M_s = 152.7^\circ\text{C}$, $A_s = 163.1^\circ\text{C}$ and $A_f = 183.6^\circ\text{C}$, where A_s and A_f indicate austenite start and finish temperatures, respectively (Figure 1a).

2.2 Microstructural Characterization

Because the microstructure of SMAs is extremely important in controlling their thermomechanical response [11, 25, 34, 57-59], in particular their fracture behavior [23, 35, 60, 61], the oxide content, the size and distribution of oxides, and other microstructural features, including the existence of H-phase precipitates [9], were investigated using scanning electron microscopy (SEM) and TEM. In Figure 2a, the backscattered electron image shows the white hafnium oxides decorating the grain boundaries. In Figure 2b, the size distribution of oxides is shown, seen to skew left with a tail to the right, indicating mostly small particles (under $1 \mu\text{m}^2$). In Figure 2c, a bright field TEM image and corresponding selected area diffraction pattern (SADP) are presented. The TEM image and the diffraction pattern do not provide an evidence for the existence of H-phase precipitation. In the bright field image, there are no clear second-phase particles, and in the SADP, there is no diffuse scattering around the martensite spots that would indicate either the precursor to the H-phase precipitates or the precipitates themselves. These images were captured on the [100] zone axis of B19'.

2.3 Uniaxial Tensile Experiments

For tensile experiments, dog-bone geometry samples, with the gage dimensions of $8 \times 3 \times 1 \text{ mm}^3$, were cut using wire Electrical Discharge Machining (EDM), and tested to failure with an engineering strain rate of $5 \times 10^{-4} \text{ s}^{-1}$ on a servo-hydraulic MTS test frame equipped with a high-temperature MTS extensometer. The extensometer was directly attached to the gage section of the samples. These samples were loaded in nominally isothermal conditions in order to determine their mechanical properties at different temperatures. The testing temperatures were decided based on the transformation temperatures so that fully martensitic,

martensitically transforming, and fully austenitic materials would all be tested. For martensitic materials, two experiments were performed below M_f ($M_f=100^\circ\text{C}$, $M_f=25^\circ\text{C}$) at 25°C and 100°C . For the samples which are martensitically transforming under stress, the experiments were performed at 160°C and 200°C ($A_s-5^\circ\text{C}$, $A_f+15^\circ\text{C}$), which are above M_s , but below M_d . For the experiments at 160°C , the samples were first heated above A_f and then cooled down to the test temperature to ensure the starting phase of the experiment is full austenite. The austenitic material was tested above M_d at 360°C ($A_f+175^\circ\text{C}$).

2.4 Fracture Toughness Experiments

Following the ASTM Standard E1820 [52], DCT specimens, with the width $W=20$ mm and the thickness $B=3.25\pm0.25$ mm, were tested at five different temperatures, 25°C , 100°C , 160°C , 200°C , and 360°C , similar to the uniaxial tension experiments, to measure the fracture toughness at different temperature regimes. The specimens were first polished on both sides with abrasive paper down to 1200 grit. The specimens were then cycled sinusoidally at 10 Hz at room temperature with an MTS servo-hydraulic frame (810 Material Test System) under load control, with the load ratio of $R=P_{min}/P_{max}=0.1$, in order to grow a fatigue pre-crack. After pre-cracking, all crack length-to-width ratios (a/W) were within the $0.45 < a/W < 0.55$ range. Two experiments were performed at each testing temperature.

For the fracture toughness experiments, the specimens were loaded in displacement control at a rate of 7.5×10^{-3} mm/s, following the procedures in ASTM Standard E1820 [52]. To capture the specimen's compliance throughout the experiments, partial unloads and reloads were performed by decreasing the displacement by 0.05 mm at 0.15 mm intervals, a range recommended by the ASTM Standard E1820. The load and crosshead displacement were recorded continuously at a rate of 10 Hz throughout the experiments. The crosshead displacement was then converted to Load Line Displacement (LLD) using a method introduced in [51], while removing the effect of machine compliance. For the experiments at elevated temperatures, the samples were heated with a Roy 1500 induction heater controlled by a Eurotherm 2200 PID temperature controller. The temperature of the sample was measured by averaging the readings from 6 K-type thermocouples directly spot-welded onto the sample. Temperatures were recorded in a LabView program through a Measurement Computing data acquisition board.

2.5 In-situ Optical Imaging

Over the course of the experiments, optical images were recorded at a rate of 1 fps using a Point Grey Blackfly camera with a Canon 18-55mm lens. These images were used to monitor the crack size and measure the 2-D strain distribution using DIC. DIC was chosen because of its non-contact nature. In order

to perform DIC, the samples were spray painted with either high-temperature-resistant black paint and speckled with white or vice versa. The imaging was performed at a resolution of 0.14 mm per pixel. The VIC-2D software, developed by Correlated Solutions, was used to calculate the full field Lagrangian strains.

3. Results and Discussion

3.1 Uniaxial Mechanical Response

The uniaxial tensile test results at different temperatures are presented in Figure 3a. Starkly different stress-strain responses near the transformation temperatures are clear, which is typical for SMAs. However, the response of the present NiTiHf HTSMA is subtly different than conventional binary NiTi SMAs, as described below. Although it is not the main focus of the current work, in the following, we briefly discuss possible deformation mechanisms that can be responsible for these differences. Understanding the deformation mechanisms during uniaxial loading at different temperatures is expected to help shed some light on the reasons for the evolution of fracture toughness with temperature (Section 3.2 below).

For the two experiments below M_f (25°C and 100°C), upon loading, the self-accommodated martensite deforms elastically before undergoing martensite reorientation/detwinning. Then, the samples fail during reorientation/ detwinning, probably before the reorientation process is completed. It is worth noting that the stress required to detwin the martensite is lower at 100°C than at 25°C. The detwinning region has a high strain hardening slope (11 ± 1 GPa), which indicates the difficulty of detwinning and likelihood of simultaneous plastic deformation. In contrast, SIM transformation region (experiments at 160°C and 200°C) features a lower strain hardening slope (5 GPa) than the detwinning region. The very high strain hardening rate observed in the deformation of the martensite phase in the present NiTiHf alloy is quite different than what is observed in binary NiTi, and it is mostly due to the difficulty of detwinning in NiTiHf HTSMAs [62, 63].

In the 160°C and 200°C cases, three stages of inelastic deformation can be distinguished. In the first stage, the austenite transforms into SIM. Upon further loading, the SIM is elastically deformed, however, in this second stage, there must be other deformation modes in play since the slope of the stress-strain curves in this stage is significantly lower than what would be expected only from elastic deformation. At the end of the second stage, the onset of a third stage is obvious at both 160°C and 200°C. However, the third stage is much clearer in the samples tested at 200°C due to the extended strain observed in this stage at 200°C. In fact, the observation of such high tensile ductility at 200°C is somewhat surprising since in general, many of the Ni-rich NiTiHf and NiTiZr compositions have not been reported to exhibit such high tensile ductility

[10, 14-17, 62]. The relatively high ductility should be a consequence of the combination of SIM, detwinning, and inelastic deformation of SIM. It is worth noting that at 200°C, upon unloading at low strain values (the first stage), the samples show perfect superelasticity (not shown here).

Lastly, in the experiments performed at 360°C, the austenite phase exhibits conventional plastic deformation behavior with decreasing strain hardening response under increasing applied strain until failure. Although it needs to be confirmed microscopically, the periodic load drops observed in the stress-strain response at 360°C (Figure 3a) can be a consequence of deformation twinning in austenite, the typical deformation mechanism observed in the austenite phase of high strength binary NiTi [62, 64-67]. From all of these stress-strain curves, it can be seen that there is a notable difference in the material behavior depending on whether the samples experience martensite reorientation/detwinning or SIM transformation – the samples strain-harden significantly more when the martensite detwins than what is observed during the SIM transformation.

3.2 Fracture Toughness Evolution as a Function of Temperature

The experimental load-displacement curves obtained from the DCT specimens are presented in Figure 3b at the same temperatures that the uniaxial mechanical responses were determined. The initial crack lengths in all specimens were $a_0=10\pm1$ mm. The load drops on the load-displacement curves come from the unload-reload sequences used to measure the compliance in cases where stable crack growth was observed. In the martensite phase (at 25°C and 100°C), unstable crack growth was observed after reaching the load maximum. In the experiments at 160°C, the material had a greater deviation from linearity and an extended displacement range beyond the load maximum before the complete failure occurred. At 200°C, the material reached a load maximum without stable crack growth, and failed in an unstable manner. In the case of the purely austenitic material (360°C), the drop from maximum load was sudden. The load drops at 25°C and 100°C were more gradual than those in the 200°C and 360°C cases.

Fracture toughness values at each testing temperature were determined from the corresponding load-displacement data, by employing the modified J -integral method as the fracture criterion, proposed in Ref. [51]. For the samples that exhibited fracture instability, *i.e.* at 25°C, 100°C, 200°C, and 360°C, the single-point J method was implemented where the J -value at the maximum load is calculated as the sum of elastic and inelastic components:

$$J = J^{el} + J^{in} = \frac{\eta^{el} A^{el}}{Bb} + \frac{\eta^{in} A^{in}}{Bb},$$

where b is the length of the unbroken ligament, A^{el} and A^{in} are the elastic and inelastic components of the area under the load-displacement curve, respectively, η^{el} and η^{in} are geometry-dependent factors.

For the samples that experienced stable crack growth, *i.e.* at 160°C, the R -curve method was used where the J -value at the i^{th} unload/reload sequence is calculated as $J_i = J_i^{el} + J_i^{in}$ where J_i^{el} and J_i^{in} are the incremental elastic and inelastic components of J_i , respectively. Also, crack extension, Δa , was calculated at each unload/reload sequence using the specimen compliance. The critical J -value was then obtained from the intersection of a regression line to J - Δa data and an offset line at 0.2 mm. More details on the aforementioned methods can be found in Ref. [51]. At 25°C, 100°C, 200°C, and 360°C, using the single point J method, an average fracture toughness J_Q of 35.3, 50.7, 56.4, and 43.1 kJ/m² were determined for these four temperatures, respectively. For the samples tested at 160°C, an average J_Q value is calculated, using the constructed R -curve (Figure 4) as 84.8 kJ/m². These J_Q values representing the fracture toughness are plotted in Figure 5a as a function of the temperature.

Up to now, all of the fracture toughness values have been designated as J_Q . The J_Q value can be qualified as geometry-independent fracture toughness, J_C , which is the material property, if the specimen meets thickness and unbroken ligament conditions, given by the equation $B, b_0 > N(J_Q/2\sigma_Y)^2$ [52], where b_0 is the initial unbroken ligament, N is a constant, which is 10 or 100, depending on if the R -curve or single point J method is used, respectively, and σ_Y is the average of the critical stress (the stress for the onset of reorientation / detwinning, the transformation, or conventional plastic yield stress), and ultimate tensile strength. The experiments at 160 and 360°C do satisfy the thickness requirements to qualify J_Q as J_C , and the experiments at all other temperatures do not.

Although the experiments at 25°C, 100°C, and 200°C do not satisfy thickness requirements according to ASTM E1820, the thickness range utilized in this study is of practical importance especially for aerospace applications [68, 69]. Therefore, this study determines the J_Q values as a function of temperature for the first time for NiTiHf HTSMAs, which can be utilized to identify the failure limits for the given thickness range. Moreover, as discussed in [70], the required thickness to ensure a thickness-independent fracture toughness for SMAs is not expected to be as stringent as the thickness requirement for conventional ductile materials. Nevertheless, further investigations on the effects of thickness on the fracture of HTSMAs are desirable.

In order to take into account the change in the elastic moduli of SMAs with temperature, the calculated J_Q values are converted to K_{JQ} values with $K_{JQ} = \sqrt{J_Q E}$, where E is the temperature dependent elastic modulus.

The K_J values are plotted as a function of temperature in Figure 5b, and all E , J_Q , and K_{JQ} values are tabulated in Table 1. Based on Figure 5, it can be seen that the SIM transformation in the present NiTiHf HTSMA clearly acts as a toughening mechanism due to the energy dissipated by martensitic transformation. This can be seen through the higher values of J_Q and K_{JQ} at 160°C and 200°C where SIM transformation occurs. SIM transformation has a greater effect on the fracture toughness at 160°C because the stress needed to start the transformation is lower at 160°C than at 200°C, which agrees with the Clausius-Clapeyron relation. Similarly, the higher fracture toughness at 100°C compared to 25°C can be explained by the lower stress required to detwin the martensite at 100°C, as mentioned in Section 3.1.

In contrast to Figure 5, in the binary equiatomic NiTi SMA [51], the fracture toughness appears to be a stepwise function as a function of temperature, i.e. the fracture toughness of martensite phase and the material that experiences SIM transformation is lower than the fracture toughness of plastically deforming austenite phase. This is the case because the crack propagates in martensite—if the material begins in austenite, it first transforms to martensite and the crack progresses through the transformed martensite region. Therefore, the measured fracture toughness represents the fracture toughness of martensite, regardless of the starting phase whether it is martensite or austenite which transforms to martensite upon loading. The fracture toughness for austenite is different above M_d because the material no longer undergoes SIM transformation.

It is believed that the reason for the differences in the fracture toughness in the present NiTiHf of the martensite phase and austenite phase, which transforms into martensite under stress in the transformation temperature range, is the difference in the energies absorbed during the reorientation/detwinning and the SIM transformation processes. In equiatomic NiTi, the detwinning process absorbs a similar amount of energy as the transformation [51], thus, similar fracture toughness values are observed. In the present NiTiHf, the strain hardening rate (11 ± 1 GPa) in the detwinning region of martensite phase is much higher than that during the transformation (5 GPa) (Figure 3a), leading to a smaller inelastic deformation zone at the crack tip. In contrast the SIM transformation leads to a higher fracture toughness and a larger inelastic deformation zone at the crack tip, as experimentally demonstrated in the next section. Under similar load values, the SIM transformation dissipates more energy as compared to the detwinning process.

3.3 Evaluation of Inelastic Deformation Zone at the Crack Tip using DIC

DIC was used to quantify the 2-D strain distributions near the crack tip. At each testing temperature, the deformed image was obtained at the onset of crack growth. For the ease of comparison, the color bar is fixed for all testing temperatures so that the red color approximates the inelastic zone. The results at

different temperatures are presented in Figure 6. As can be seen in the figure, at 25°C, the inelastic zone is relatively small, which matches with the trends in Figure 5. At 100°C, there is an increase in the size of the inelastic deformation zone. At 160°C, there is a noticeable increase in the inelastic zone size, due to the SIM transformation. This can be rationalized using the observations in the uniaxial stress-strain response at 160°C, according to which the inelastic deformation mechanism, in this case, martensitic transformation, starts at a significantly lower stress/strain values compared to the detwinning mechanism in martensite. At 200°C, the transformation zone becomes relatively small because at this temperature the transformation is triggered at a higher stress value. Lastly, at 360°C, the inelastic deformation zone is comparable in size to that at 25°C.

Comparing the DIC results to the fracture toughness values, one can see that the trend in the temperature evolution in the inelastic deformation zone size matches well with the temperature evolution of the fracture toughness values. This explains the higher fracture toughness value for the samples undergoing SIM transformation, especially at 160°C, where the material undergoes phase transformation at early stages of loading (Figure 3a) and dissipates much more energy than martensite detwinning and plastic deformation of austenite.

3.4 Comparison of Fracture Surfaces from Different Temperature Failures

The fracture surfaces of the all failed DCT samples were investigated using SEM at room temperature in order to identify the signature fracture characteristics. The results are presented in Figure 7. It can be seen that there is a difference in the fracture surface morphology at different testing temperatures, which is characterized by either cleavage or micro-void coalescence, or a combination of both. At lower temperatures (25 and 100 °C), the fracture surfaces are much flatter, evidence of quasi-cleavage, transgranular fracture (Figure 7a). As the temperature increases into the range where SIM transformation takes place (at 160°C), the fracture surfaces become dimpled and show evidence of ductile fracture (Figure 7b). As the temperature increases to 200°C and 360°C, the fracture surfaces show increasing characteristics of intergranular fracture (Figure 7c and d), likely to be along the austenite grain boundaries. The repeating structures on the fracture surface which look like parallel bands in these figures, should be bundles of martensite lathes, based on the martensite twin size observed in Figure 2, that form upon cooling down from the austenitic phase, as these SEM micrographs were taken at room temperature, and not at the temperature of the fracture toughness experiments. Overall, the fracture surface morphologies follow the same temperature trends observed in the fracture toughness experiments and DIC observations, where the SIM transformation leads to the most energy dissipation during the crack growth.

4. Summary and Conclusions

In the present study, the fracture behavior of a Ni-rich $\text{Ni}_{50.3}\text{Ti}_{29.7}\text{Hf}_{20}$ (at. %) HTSMA was investigated at different temperatures using disk-shaped compact tension specimens: below M_f , above M_s but below M_d , and above M_d , in order to determine the fracture toughnesses of martensitic, martensitically transforming austenitic, and plastically deforming austenitic phases, respectively. Fracture behavior was observed to be highly temperature/phase dependent. The stress-induced martensite (SIM) transformation was found to be a toughening mechanism, increasing the fracture toughness in the present NiTiHf HTSMA, and resulting in stable crack growth when the temperature is close to M_s . This is in contrast to the fracture toughness values of similar phases in binary equiatomic NiTi SMAs, where martensitic and martensitically transforming austenitic phases experience the same fracture toughness values near the transformation temperatures while plastically deforming austenitic phase exhibits much higher fracture toughness. The apparent toughening via the SIM transformation in the NiTiHf HTSMA is due to the differences in the strain hardening behavior of the martensite detwinning, SIM transformation, and austenite plastic deformation regimes, leading to different sizes of inelastic deformation zones at the crack tip and thus different energy dissipation levels. This toughening mechanism is less significant when the stress required for SIM transformation is higher at higher temperatures. Digital Image Correlation was implemented to monitor the extent of the inelastic deformation zones near the crack tip, which match well with the observations in temperature evolution of the fracture toughness values. The inelastic zones at temperatures where the SIM transformation is active before failure were found to be larger than at temperatures where only one phase is present, or the stress required to form SIM is very high.

Acknowledgements

This study was supported by the US Air Force Office of Scientific Research, under Grant no. FA9550-18-1-0276 and the National Science Foundation under Grant no. CMMI-1917367. B. Young acknowledges the support from the 2017 SMST Fellowship. The authors also acknowledge the NASA Glenn Research Center for providing the material used in this work. The authors acknowledge Dr. Baxevanis for the valuable discussions on the fracture toughness measurement method.

References

- [1] D.C. Lagoudas, Shape memory alloys: modeling and engineering applications Springer Science & Business Media 2008.
- [2] D.J. Hartl, D.C. Lagoudas, Aerospace applications of shape memory alloys, Proceedings of the Institution of Mechanical Engineers, Part G: Journal of Aerospace Engineering 221(4) (2007) 535-552.
- [3] H. Tobushi, K. Kimura, H. Iwanaga, J.R. Cahoon, Basic research on shape memory alloy heat engine (output power characteristics and problems in development), JSME International Journal 33 (1990).
- [4] W.J. Buehler, J.V. Gilfrich, R.C. Wiley, Effect of low-temperature phase changes on the mechanical properties of alloys near composition TiNi, Journal of Applied Physics 34(5) (1963) 1475-1477.
- [5] T. Umale, D. Salas, B. Tomes, R. Arroyave, I. Karaman, The effects of wide range of compositional changes on the martensitic transformation characteristics of NiTiHf shape memory alloys, Scripta Materialia 161 (2019) 78-83.
- [6] J. Ma, I. Karaman, R.D. Noebe, High temperature shape memory alloys, International Materials Reviews 55(5) (2010) 257-315.
- [7] O. Benafan, R.D. Noebe, S.A. Padula, R. Vaidyanathan, Microstructural response during isothermal and isobaric loading of a precipitation-strengthened Ni29.7-Ti-20Hf high-temperature shape memory alloy, Metallurgical and Materials Transactions A 43(12) (2012) 4539-4552.
- [8] S.M. Saghalian, H.E. Karaca, H. Tobe, M. Souri, R. Noebe, Y.I. Chumlyakov, Effects of aging on the shape memory behavior of Ni-rich Ni_{50.3}Ti_{29.7}Hf₂₀ single crystals, Acta Materialia 87 (2015) 128-141.
- [9] R. Santamarta, R. Arróyave, J. Pons, A. Evirgen, I. Karaman, H.E. Karaca, R.D. Noebe, TEM study of structural and microstructural characteristics of a precipitate phase in Ni-rich Ni-Ti-Hf and Ni-Ti-Zr shape memory alloys, Acta Materialia 61(16) (2013) 6191-6206.
- [10] A. Evirgen, Microstructural characterization and shape memory response of Ni-Rich NiTiHf and NiTiZr high temperature Shape Memory Alloys, 2014.
- [11] M. Belbasi, M.T. Salehi, Influence of chemical composition and melting process on hot rolling of NiTiHf shape memory alloy, Journal of Materials Engineering and Performance 23(7) (2014) 2368-2372.
- [12] G.S. Bigelow, A. Garg, S.A. Padula, D.J. Gaydosh, R.D. Noebe, Load-biased shape-memory and superelastic properties of a precipitation strengthened high-temperature Ni_{50.3}Ti_{29.7}Hf₂₀ alloy, Scripta Materialia 64(8) (2011) 725-728.
- [13] A. Evirgen, J. Pons, I. Karaman, R. Santamarta, R.D. Noebe, H-Phase precipitation and martensitic transformation in Ni-rich Ni-Ti-Hf and Ni-Ti-Zr high-temperature shape memory alloys, Shape Memory and Superelasticity 4(1) (2018) 85-92.
- [14] A. Evirgen, I. Karaman, R. Santamarta, J. Pons, C. Hayrettin, R.D. Noebe, Relationship between crystallographic compatibility and thermal hysteresis in Ni-rich NiTiHf and NiTiZr high temperature shape memory alloys, Acta Materialia 121 (2016) 374-383.
- [15] A. Evirgen, I. Karaman, R. Santamarta, J. Pons, R.D. Noebe, Microstructural characterization and shape memory characteristics of the Ni_{50.3}Ti_{34.7}Hf₁₅ shape memory alloy, Acta Materialia 83 (2015) 48-60.
- [16] A. Evirgen, I. Karaman, R.D. Noebe, R. Santamarta, J. Pons, Effect of precipitation on the microstructure and the shape memory response of the Ni_{50.3}Ti_{29.7}Zr₂₀ high temperature shape memory alloy, Scripta Materialia 69(5) (2013) 354-357.
- [17] A. Evirgen, F. Basner, I. Karaman, R.D. Noebe, J. Pons, R. Santamarta, Effect of aging on the martensitic transformation characteristics of a Ni-rich NiTiHf high temperature shape memory alloy, Functional Materials Letters 05(04) (2012) 1250038.
- [18] H.E. Karaca, E. Acar, H. Tobe, S.M. Saghalian, NiTiHf-based shape memory alloys, Materials Science and Technology 30(13) (2014) 1530-1544.
- [19] S.M. Saghalian, H.E. Karaca, M. Souri, A.S. Turabi, R.D. Noebe, Tensile shape memory behavior of Ni_{50.3}Ti_{29.7}Hf₂₀ high temperature shape memory alloys, Materials & Design 101 (2016) 340-345.
- [20] D. Shukla, R.D. Noebe, P. Stebner Aaron, Empirical study of the multiaxial, thermomechanical behavior of NiTiHf shape memory alloys, (2013).

[21] O. Benafan, Deformation and phase transformation processes in polycrystalline NiTi and NiTiHf high temperature shape memory alloys, (2012) Doctoral Dissertation, University of Central Florida.

[22] C. Hayrettin, Actuation fatigue and fracture of shape memory alloys, Materials Science and Engineering, (2017) Doctoral Dissertation, Texas A&M University.

[23] O. Karakoc, A. Demblon, R.W. Wheeler, D.C. Lagoudas, I. Karaman, Effects of testing parameters on the fatigue performance NiTiHf high temperature shape memory alloys, AIAA Scitech 2019 Forum, 2019, p. 0416.

[24] O. Karakoc, C. Hayrettin, D. Canadinc, I. Karaman, Role of applied stress level on the actuation fatigue behavior of NiTiHf high temperature shape memory alloys, *Acta Materialia* 153 (2018) 156-168.

[25] O. Karakoc, C. Hayrettin, A. Evirgen, R. Santamarta, D. Canadinc, R.W. Wheeler, S.J. Wang, D.C. Lagoudas, I. Karaman, Role of microstructure on the actuation fatigue performance of Ni-Rich NiTiHf high temperature shape memory alloys, *Acta Materialia* 175 (2019) 107-120.

[26] C. Hayrettin, O. Karakoc, I. Karaman, J.H. Mabe, R. Santamarta, J. Pons, Two way shape memory effect in NiTiHf high temperature shape memory alloy tubes, *Acta Materialia* 163 (2019) 1-13.

[27] S.M. Russell, F. Sczerzenie, Engineering considerations in the application of NiTiHf and NiAl as practical high-temperature shape memory alloys, *MRS Proceedings* 360 (1994) 455.

[28] N. Babacan, M. Bilal, C. Hayrettin, J. Liu, O. Benafan, I. Karaman, Effects of cold and warm rolling on the shape memory response of Ni₅₀Ti₃₀Hf₂₀ high-temperature shape memory alloy, *Acta Materialia* 157 (2018) 228-244.

[29] B. Kockar, I. Karaman, J.I. Kim, Y. Chumlyakov, A method to enhance cyclic reversibility of NiTiHf high temperature shape memory alloys, *Scripta Materialia* 54(12) (2006) 2203-2208.

[30] M. Moholt, O. Benafan, Spanwise Adaptive Wing, Presented at the 3rd Annual Concergent Aeronautics Solutions Showcase and Innovation Faire, VA (2017).

[31] R.L. Holtz, K. Sadananda, M.A. Imam, Fatigue thresholds of Ni-Ti alloy near the shape memory transition temperature, *International Journal of Fatigue* 21 (1999) S137-S145.

[32] S.W. Robertson, R.O. Ritchie, In vitro fatigue-crack growth and fracture toughness behavior of thin-walled superelastic Nitinol tube for endovascular stents: A basis for defining the effect of crack-like defects, *Biomaterials* 28(4) (2007) 700-709.

[33] S. Daly, A. Miller, G. Ravichandran, K. Bhattacharya, An experimental investigation of crack initiation in thin sheets of nitinol, *Acta Materialia* 55(18) (2007) 6322-6330.

[34] S. Gollerthan, M.L. Young, A. Baruj, J. Frenzel, W.W. Schmahl, G. Eggeler, Fracture mechanics and microstructure in NiTi shape memory alloys, *Acta Materialia* 57(4) (2009) 1015-1025.

[35] A. Ahadi, Q. Sun, Grain size dependence of fracture toughness and crack-growth resistance of superelastic NiTi, *Scripta Materialia* 113 (2016) 171-175.

[36] B. Katanchi, N. Choupani, J. Khalil-Allafi, R. Tavangar, M. Baghani, Mixed-mode fracture of a superelastic NiTi alloy: Experimental and numerical investigations, *Engineering Fracture Mechanics* 190 (2018) 273-287.

[37] S.W. Robertson, A.R. Pelton, R.O. Ritchie, Mechanical fatigue and fracture of Nitinol, *International Materials Reviews* 57(1) (2012) 1-37.

[38] C. Maletta, E. Sgambitterra, F. Furgiuele, Crack tip stress distribution and stress intensity factor in shape memory alloys, 36(9) (2013) 903-912.

[39] K.N. Melton, O. Mercier, The mechanical properties of NiTi-based shape memory alloys, *Acta Metallurgica* 29(2) (1981) 393-398.

[40] S.W. Robertson, R.O. Ritchie, A fracture-mechanics-based approach to fracture control in biomedical devices manufactured from superelastic Nitinol tube, *Journal of Biomedical Materials Research Part B: Applied Biomaterials* 84B(1) (2008) 26-33.

[41] J. Luo, J. He, X. Wan, T. Dong, Y. Cui, X. Xiong, Fracture properties of polycrystalline NiTi shape memory alloy, *Materials Science and Engineering: A* 653 (2016) 122-128.

[42] ASTM Standard E399, Standard test method for linear-elastic plane-strain fracture toughness K_{Ic} of metallic materials, 2011. ASTM International, West Conshohocken, PA.

[43] T. Baxevanis, Y. Chemisky, D.C. Lagoudas, Finite element analysis of the plane strain crack-tip mechanical fields in pseudoelastic shape memory alloys, *Smart Materials and Structures* 21(9) (2012) 094012.

[44] T. Baxevanis, D. Lagoudas, A mode I fracture analysis of a center-cracked infinite shape memory alloy plate under plane stress, *International Journal of Fracture* 175(2) (2012) 151-166.

[45] A. Falvo, F. Furgiuele, A. Leonardi, C. Maletta, Stress-Induced Martensitic Transformation in the Crack Tip Region of a NiTi Alloy, *Journal of Materials Engineering and Performance* 18(5) (2009) 679-685.

[46] B. Haghgouyan, S. Jape, T. Baxevanis, I. Karaman, D.C. Lagoudas, Stable crack growth in NiTi shape memory alloys: 3D finite element modeling and experimental validation, *Smart Materials and Structures* 28(6) (2019) 064001.

[47] B. Haghgouyan, I. Karaman, S. Jape, A. Solomou, D.C. Lagoudas, Crack Growth Behavior in NiTi Shape Memory Alloys Under Mode-I Isothermal Loading: Effect of Stress State, 2018.

[48] S. Jape, T. Baxevanis, D.C. Lagoudas, Stable Crack Growth During Thermal Actuation of Shape Memory Alloys, *Shape Memory and Superelasticity* 2(1) (2016) 104-113.

[49] E. Sgambitterra, C. Maletta, F. Furgiuele, H. Sehitoglu, Fatigue crack propagation in [0 1 2] NiTi single crystal alloy, *International Journal of Fatigue* 112 (2018) 9-20.

[50] E. Sgambitterra, C. Maletta, P. Magarò, D. Renzo, F. Furgiuele, H. Sehitoglu, Effects of Temperature on Fatigue Crack Propagation in Pseudoelastic NiTi Shape Memory Alloys, *Shape Memory and Superelasticity* (2019).

[51] B. Haghgouyan, C. Hayrettin, T. Baxevanis, I. Karaman, D.C. Lagoudas, Fracture toughness of NiTi—Towards establishing standard test methods for phase transforming materials, *Acta Materialia* 162 (2019) 226-238.

[52] ASTM Standard E1820, Standard Test Method for Measurement of Fracture Toughness, 2014. ASTM International, West Conshohocken, PA.

[53] B. Haghgouyan, N. Shafaghi, C.C. Aydiner, G. Anlas, Experimental and computational investigation of the effect of phase transformation on fracture parameters of an SMA, *Smart Materials and Structures* 25(7) (2016) 075010.

[54] C. Maletta, E. Sgambitterra, F. Niccoli, Temperature dependent fracture properties of shape memory alloys: novel findings and a comprehensive model, *Scientific Reports* 6(1) (2016) 17.

[55] B. Haghgouyan, B. Young, I. Karaman, D.C. Lagoudas, Fracture toughness of martensitic NiTiHf high-temperature shape memory alloy, SPIE2019.

[56] B. Amin-Ahmadi, R.D. Noebe, A.P. Stebner, Crack propagation mechanisms of an aged nickel-titanium-hafnium shape memory alloy, *Scripta Materialia* 159 (2019) 85-88.

[57] Y. Chen, O. Tyc, O. Molnárová, L. Heller, P. Šittner, Tensile Deformation of Superelastic NiTi Wires in Wide Temperature and Microstructure Ranges, *Shape Memory and Superelasticity* 5(1) (2019) 42-62.

[58] P.P. Paul, M. Fortman, H.M. Paranjape, P.M. Anderson, A.P. Stebner, L.C. Brinson, Influence of Structure and Microstructure on Deformation Localization and Crack Growth in NiTi Shape Memory Alloys, *Shape Memory and Superelasticity* 4(2) (2018) 285-293.

[59] R. Santamarta, A. Evirgen, A.M. Perez-Sierra, J. Pons, E. Cesari, I. Karaman, R.D. Noebe, Effect of Thermal Treatments on Ni–Mn–Ga and Ni–Rich Ni–Ti–Hf/Zr High-Temperature Shape Memory Alloys, *Shape Memory and Superelasticity* 1(4) (2015) 418-428.

[60] K. Gall, N. Yang, H. Sehitoglu, Y.I. Chumlyakov, Fracture of precipitated NiTi shape memory alloys, *International Journal of Fracture* 109(2) (2001) 189-207.

[61] S.W. Robertson, A. Mehta, A.R. Pelton, R.O. Ritchie, Evolution of crack-tip transformation zones in superelastic Nitinol subjected to in situ fatigue: A fracture mechanics and synchrotron X-ray microdiffraction analysis, *Acta Materialia* 55(18) (2007) 6198-6207.

[62] H.E. Karaca, S.M. Saghaian, G. Ded, H. Tobe, B. Basaran, H.J. Maier, R.D. Noebe, Y.I. Chumlyakov, Effects of nanoprecipitation on the shape memory and material properties of an Ni-rich NiTiHf high temperature shape memory alloy, *Acta Materialia* 61(19) (2013) 7422-7431.

[63] O. Benafan, A. Garg, R.D. Noebe, G.S. Bigelow, S.A. Padula, D.J. Gaydosh, N. Schell, J.H. Mabe, R. Vaidyanathan, Mechanical and functional behavior of a Ni-rich $\text{Ni}_{50.3}\text{Ti}_{29.7}\text{Hf}_{20}$ high temperature shape memory alloy, *Intermetallics* 50 (2014) 94-107.

[64] N.S. Surikova, Y.I. Chumlyakov, Mechanisms of plastic deformation of the titanium nickelide single crystals, *Physics of Metals and Metallography* 89(2) (2000) 196-205.

[65] H. Sehitoglu, I. Karaman, R. Anderson, X. Zhang, K. Gall, H.J. Maier, Y. Chumlyakov, Compressive response of NiTi single crystals, *Acta Materialia* 48(13) (2000) 3311-3326.

[66] H. Sehitoglu, R. Hamilton, D. Canadinc, X.Y. Zhang, K. Gall, I. Karaman, Y. Chumlyakov, H.J. Maier, Detwinning in NiTi alloys, *Metallurgical and Materials Transactions A* 34(1) (2003) 5-13.

[67] Y.I. Chumlyakov, I.V. Kireeva, E.Y. Panchenko, E.E. Timofeeva, Z.V. Pobedennaya, S.V. Chusov, I. Karaman, H. Maier, E. Cesari, V.A. Kirillov, High-temperature superelasticity in CoNiGa, CoNiAl, NiFeGa, and TiNi monocrystals, *Russian Physics Journal* 51(10) (2008) 1016-1036.

[68] O. Benafan, D.J. Gaydosh, High temperature shape memory alloy $\text{Ni}_{50.3}\text{Ti}_{29.7}\text{Hf}_{20}$ torque tube actuators, *Smart Materials and Structures* 26(9) (2017) 095002.

[69] O. Benafan, D.J. Gaydosh, Constant-torque thermal cycling and two-way shape memory effect in $\text{Ni}_{50.3}\text{Ti}_{29.7}\text{Hf}_{20}$ torque tubes, *Smart Materials and Structures* 27(7) (2018) 075035.

[70] J. Makkar, T. Baxevanis, Notes on the Experimental Measurement of Fracture Toughness of Shape Memory Alloys, *Journal of Intelligent Material Systems and Structures*, 1-9 (2019).

FIGURES AND TABLES

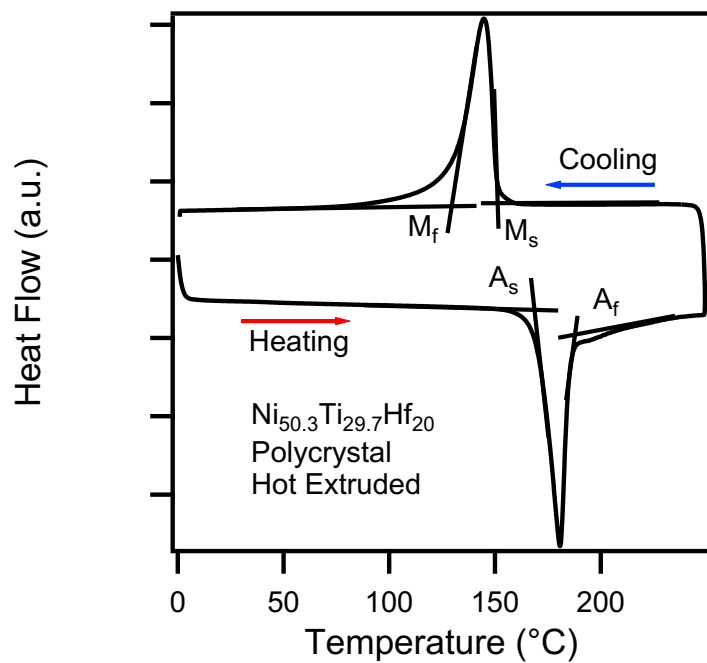


Figure 1. Differential Scanning Calorimetry of a hot extruded, polycrystalline Ni_{50.3}Ti_{29.7}Hf₂₀ high temperature shape memory alloy, revealing transformation temperatures to be M_f=125.6, M_s=152.7, A_s=163.1, A_f=183.6°C.

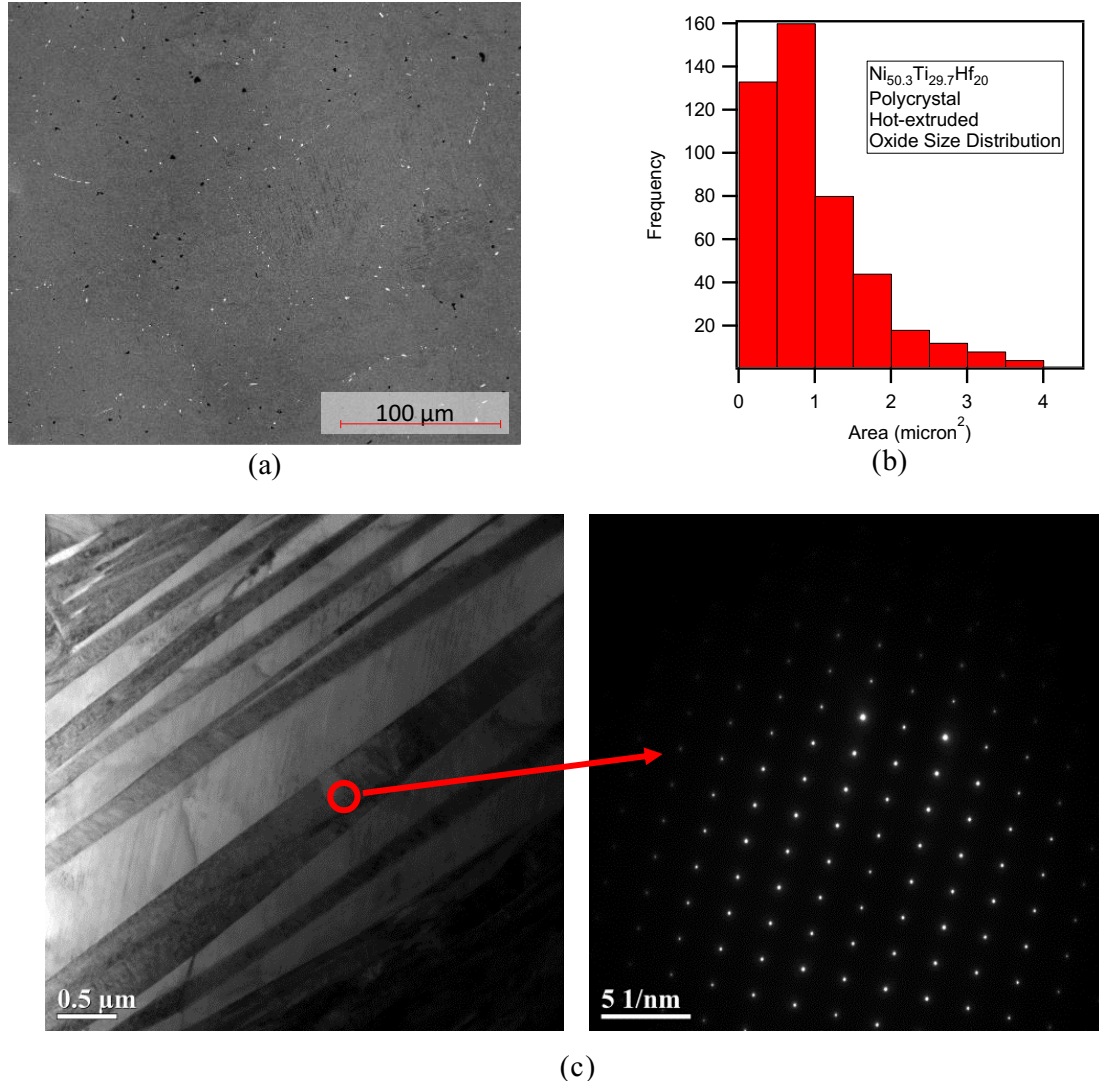


Figure 2. (a) A back scattered electron image of the hot extruded, polycrystalline Ni_{50.3}Ti_{29.7}Hf₂₀ high temperature shape memory alloy. Hafnium oxides are seen in white, decorating the grain boundaries of the sample; (b) the size and frequency of the oxide distribution, showing a skewed distribution with a tail to the right; (c) the bright field TEM image, taken on the [100] zone axis, of martensite lathes and corresponding selected area diffraction pattern (SADP). Neither the bright field image nor the SADP show any indication of precipitates.

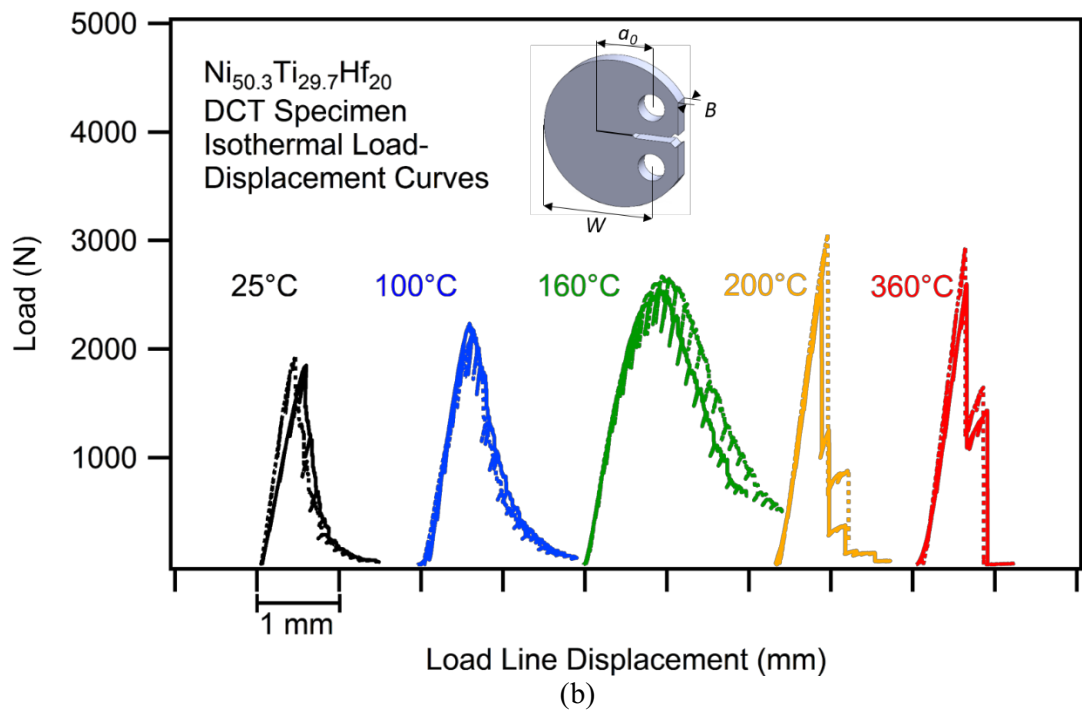
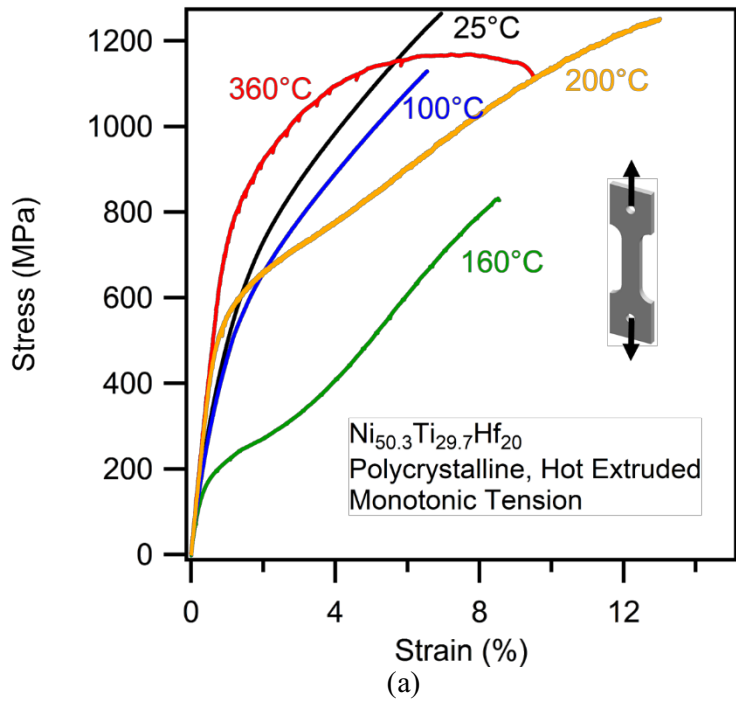


Figure 3. Uniaxial tension and mode-I fracture toughness results of hot extruded, polycrystalline $\text{Ni}_{50.3}\text{Ti}_{29.7}\text{Hf}_{20}$ high temperature shape memory alloy at 25°C ($M_f=100^\circ\text{C}$), 100°C ($M_f=25^\circ\text{C}$), 160°C ($A_f=5^\circ\text{C}$), 200°C ($A_f+15^\circ\text{C}$), and 360°C ($A_f+175^\circ\text{C}$): (a) stress-strain response of dog-bone shaped specimens under tension; (b) load-displacement response of the disk-shaped compact tension (DCT) specimens (thickness $B=3.25\pm0.25$ mm, width $W=20$ mm, initial crack length $a_0=10\pm1$ mm).

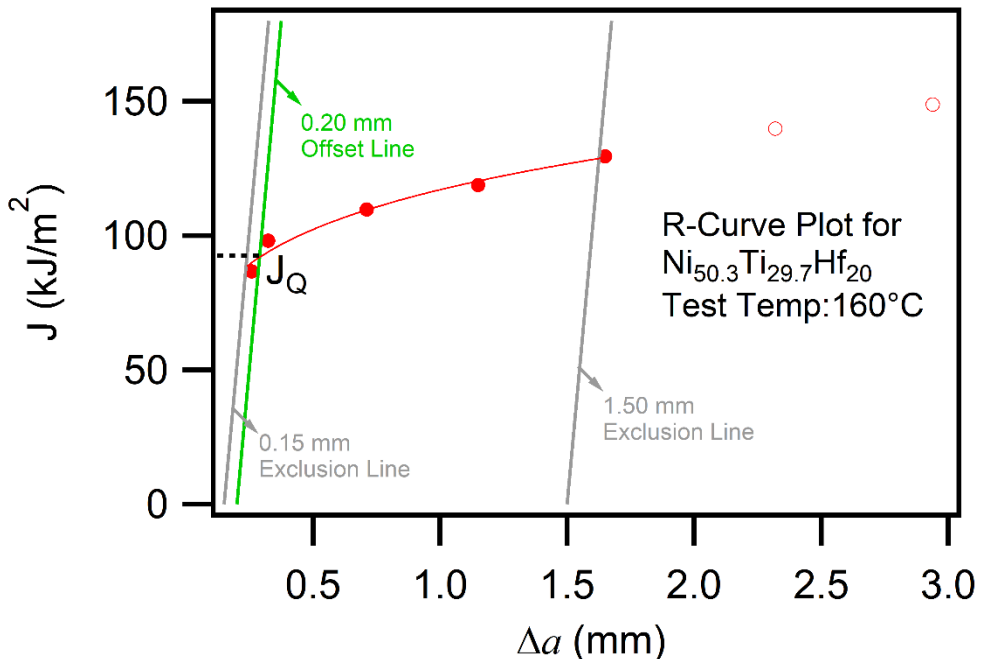
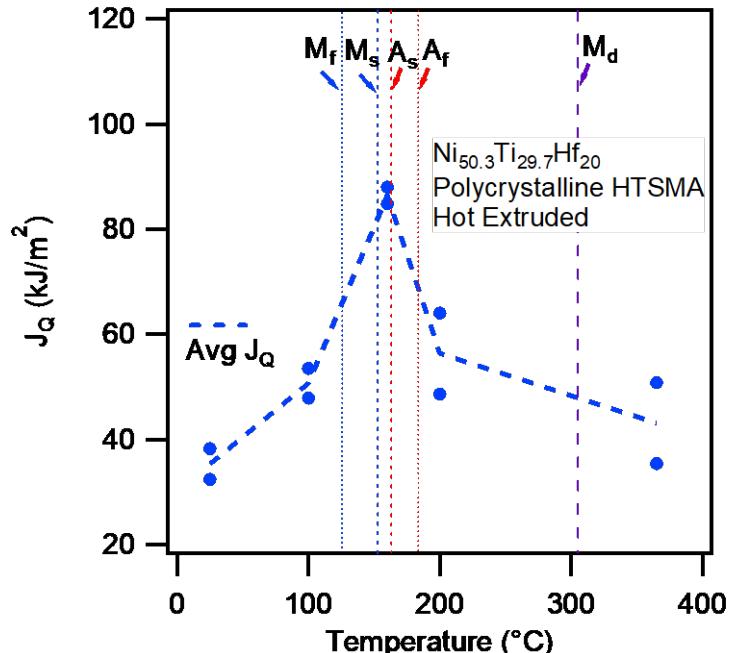
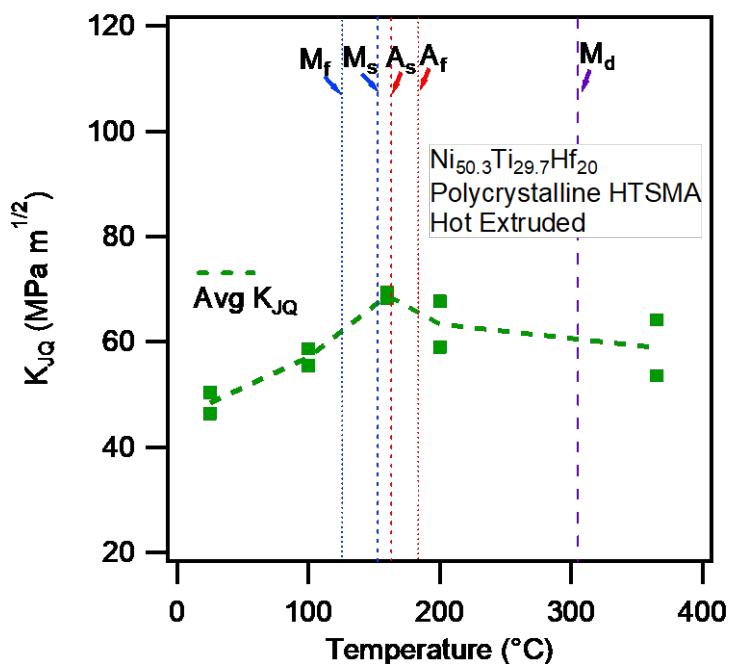


Figure 4. R-curve construction for the fracture toughness experiment at 160°C for the hot extruded, polycrystalline $\text{Ni}_{50.3}\text{Ti}_{29.7}\text{Hf}_{20}$ high temperature shape memory alloy. The critical value of J_Q , shown by the dashed line, is obtained from taking the intercept of a power law regression line of the J - Δa data and a 0.2 mm offset line with a slope of $2\sigma_Y$. Here σ_Y is the average of the transformation stress and ultimate tensile strength at the test temperature. Points to the left of the 0.15 mm exclusion line and to the right of the 1.50 mm exclusion line are not used for regression analysis to obtain the power law regression line.



(a)



(b)

Figure 5. (a) Fracture toughness J_Q vs. temperature; and (b) fracture toughness K_{JQ} vs. temperature for the hot extruded, polycrystalline $\text{Ni}_{50.3}\text{Ti}_{29.7}\text{Hf}_{20}$ high temperature shape memory alloy. See text for detailed description of how these values were determined from the load displacement curves in Figure 3b. The SIM transformation appears to have a toughening effect on the fracture toughness in both J_Q and K_{JQ} . The material at 200°C has a less pronounced toughening effect because the stress required to induce transformation at that temperature is higher than that at 160°C.

Table 1: Apparent elastic modulus (E), average J_Q , and average K_{JQ} values at different test temperatures for the hot extruded, polycrystalline $\text{Ni}_{50.3}\text{Ti}_{29.7}\text{Hf}_{20}$ high temperature shape memory alloy.

Temperature (°C)	E (GPa)	J_Q (kJ/m ²)	K_{JQ} (MPa $\sqrt{\text{m}}$)
25	66.4	35.3	48.4
100	64.3	50.7	57.1
160	54.8	86.4	68.0
200	71.6	56.4	63.4
360	81.1	43.1	58.9

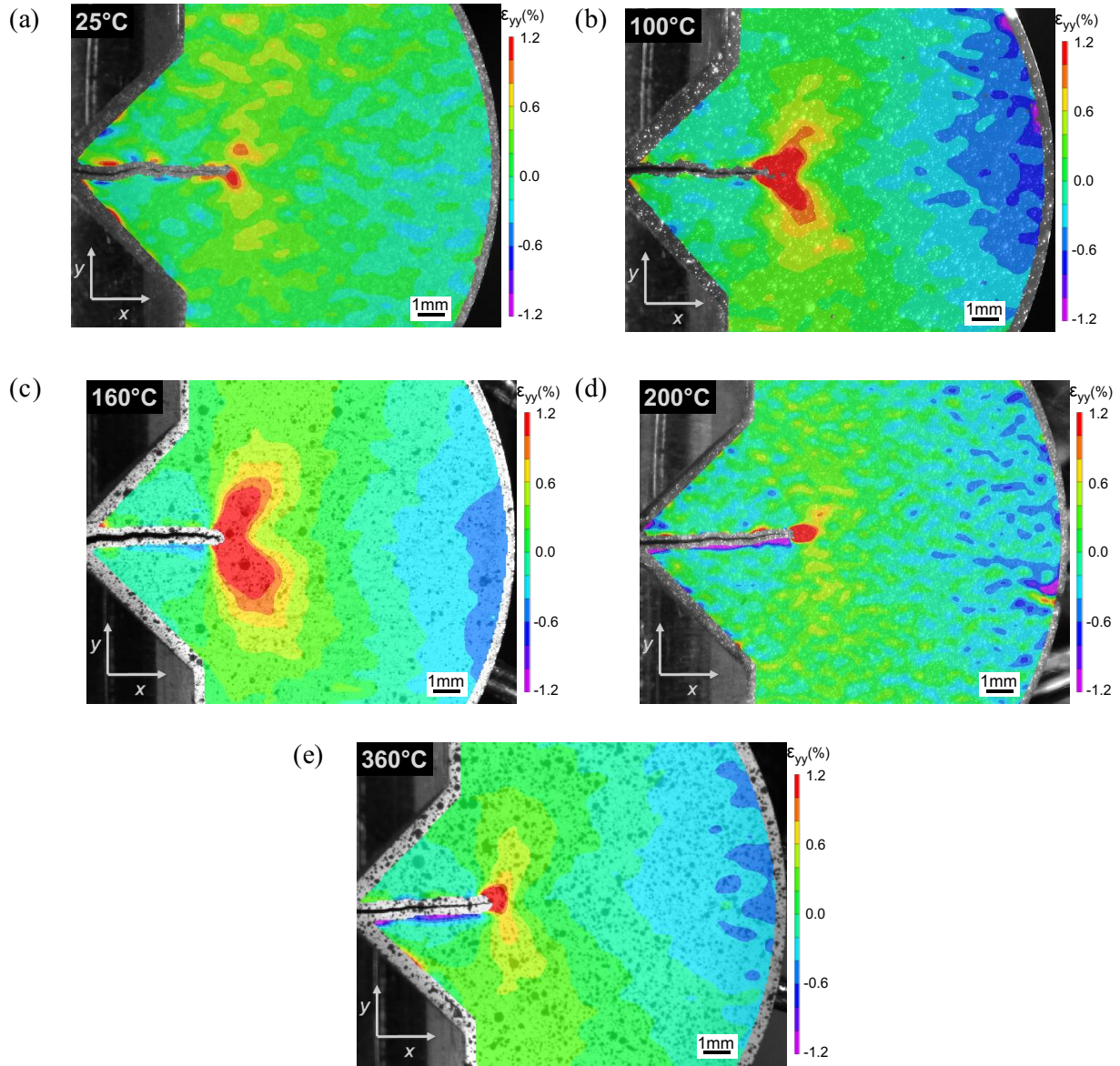


Figure 6. Strain (ϵ_{yy}) contour plots at the onset of crack growth for the DCT specimens of the hot extruded, polycrystalline $\text{Ni}_{50.3}\text{Ti}_{29.7}\text{Hf}_{20}$ high temperature shape memory alloy, obtained using DIC at different test temperatures: (a) 25°C , (b) 100°C , (c) 160°C , (d) 200°C , and (e) 360°C . For the ease of comparison, the color bar is fixed for all temperatures so that the red color approximates the inelastic zone.

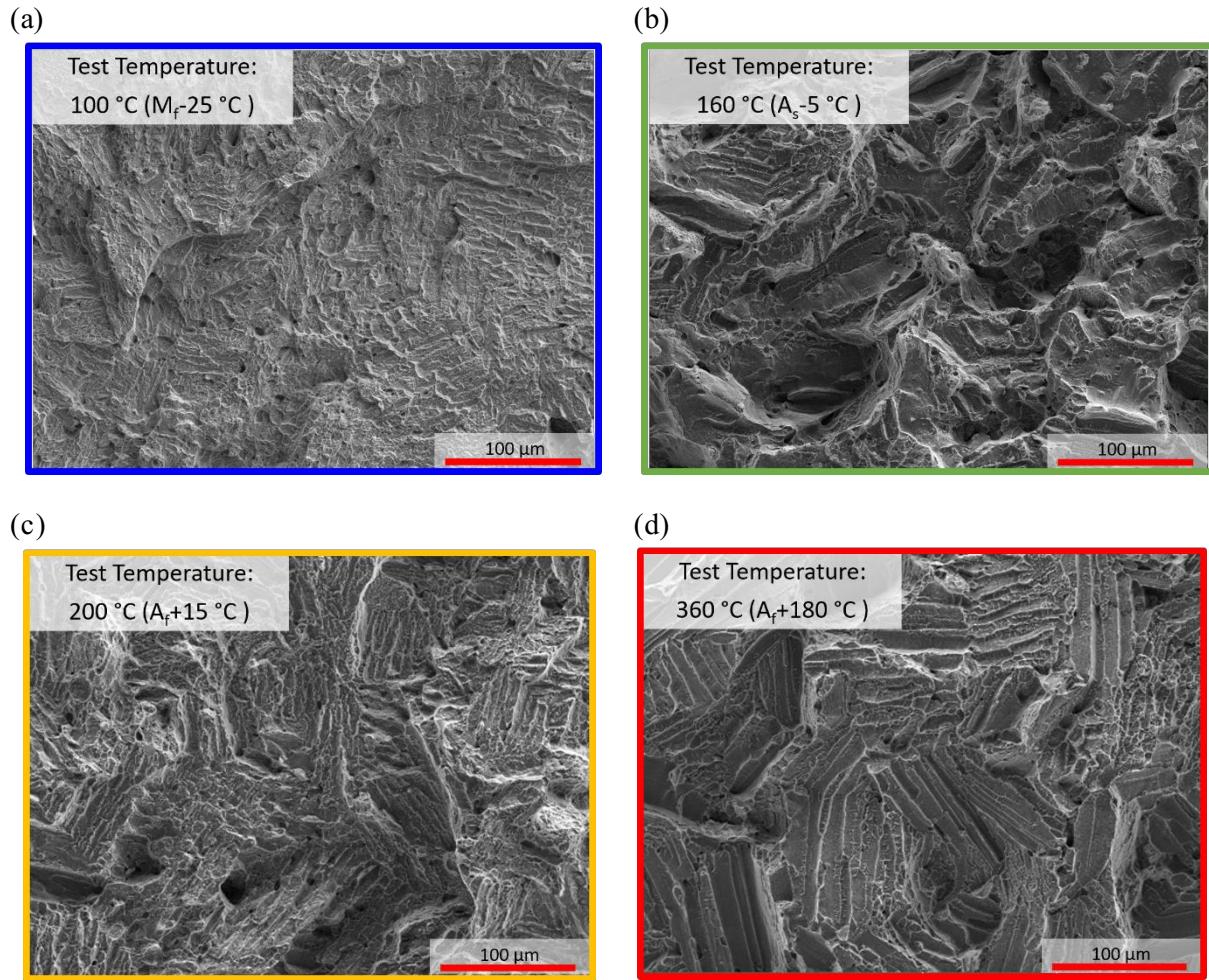


Figure 7. Fracture surfaces of the hot extruded, polycrystalline $\text{Ni}_{50.3}\text{Ti}_{29.7}\text{Hf}_{20}$ DCT specimens taken using an SEM at room temperature: (a) in the samples tested at 100°C, the fracture surface is relatively flat indicating quasi-cleavage fracture; (b) for the samples tested at 160°C, the fracture surface features noticeably more dimples indicating much higher energy dissipation for fracture; (c) for the 200°C samples, the surfaces seem to exhibit a striated pattern, which is believed to be martensite lathes forming upon cooling inside the larger austenite grains; and (d) for the samples tested at 360°C, the surface is jagged, and has evidence of inter-granular fracture.